THE ASTROPHYSICAL JOURNAL, 470:1172–1186, 1996 October 20

GODDARD HIGH RESOLUTION SPECTROGRAPH OBSERVATIONS OF VARIABILITY IN THE RS CANUM VENATICORUM SYSTEM V711 TAURI (HR 1099)[1]

ROBERT C. DEMPSEY
Astronomy Programs, Computer Sciences Corporation, Space Telescope Science Institute, 3700 San Martin Drive, Baltimore, MD 21218; dempsey@stsci.edu

JAMES E. NEFF AND MARJORIE J. THORPE
The Pennsylvania State University, Department of Astronomy and Astrophysics, 525 Davey Lab, University Park, PA 16802

JEFFREY L. LINSKY
JILA, University of Colorado Boulder, CO 80309-0440

ALEXANDER BROWN[2]
Center for Astrophysics & Space Astronomy, University of Colorado Boulder, CO 80309-0389

GIUSEPPE CUTISPOTO
Catania Astrophysical Observatory, viale A. Doria 6, I-95125 Catania, Italy

AND

MARCELLO RODONÒ
Institute of Astronomy, University of Catania, & Catania Astrophysical Observatory, viale A. Doria 6, I-95125 Catania, Italy
Received 1996 March 4; accepted 1996 May 15

ABSTRACT

Goddard High Resolution Spectrograph (GHRS) observations of the RS CVn–type binary V711 Tau (K1 IV+G5 IV) were obtained at several phases over two consecutive stellar orbital cycles in order to study ultraviolet emission-line profile and flux variability. Spectra cover the Mg II *h* and *k* lines, C IV doublet, and Si IV region, as well as the density-sensitive lines of C III] (1909 Å) and Si III] (1892 Å). *IUE* spectra, EUV data, and *UBV* photometry were obtained contemporaneously with the GHRS data. Variable extended wings were detected in the Mg II lines. We discuss the Mg II line profile variability using various Gaussian emission profile models. No rotational modulation of the line profiles was observed, but there were several large flares. These flares produced enhanced emission in the extended line wings, radial velocity shifts, and asymmetries in some line profiles. Nearly continuous flaring for more than 24 hr, as indicated in the *IUE* data, represents the most energetic and long-lived chromospheric and transition region flare ever observed with a total energy much greater than 5×10^{35} ergs. The C III] to Si III] line ratio is used to estimate the plasma density during the flares.

Subject headings: line: profiles — stars: chromospheres — stars: flare — stars: individual (V711 Tauri) — ultraviolet: stars

1. INTRODUCTION

Late-type stars in short-period binary systems display a rich variety of phenomena reminiscent of solar activity—dark starspots, luminous X-ray and UV emissions, powerful nonthermal radio sources, and highly energetic flares—with energies and physical dimensions orders of magnitude larger than on the Sun (Linsky 1990). The physical processes or scale lengths could be quite different than those on the Sun. Cool stars in short-period binaries are more active than single stars of similar mass and age, primarily owing to tidally induced rapid synchronous rotation. Such is the case among the RS Canum Venaticorum (RS CVn) systems, which are detached binaries where one or both stars are G or K subgiants.

Sunspots are covered by regions that appear bright in UV emission lines. These "active regions" or "plages" have magnetic fluxes 10–100 times larger than the quiet solar photosphere. Similarly, several RS CVn systems display anticorrelated ultraviolet (UV) emission and visual brightness, in which maximum UV emission occurs at photometric minimum (e.g., Baliunas & Dupree 1982; Marstad et al. 1982; Rodonò et al. 1987; Zirin 1988). However, as detailed by Hallam, Altner, & Endal (1991), different UV transitions exhibit slightly disparate behavior because each line is formed at a different height in the chromosphere.

Very high quality spectra and new data analysis techniques now permit the determination of the spatial structure (i.e., size, location, temperature) of spots and plages on stars other than the Sun. Phase-dependent distortions of line profiles can result from discrete hot or cool regions crossing the visible hemisphere of the star as it rotates. Doppler imaging (DI) and correlative analysis are tools that allow the interpretation of the surface inhomogeneities that produce such profile asymmetries (Vogt & Penrod 1983; Dempsey et al. 1992). Walter et al. (1987) and Neff et al. (1989) have applied similar spectral imaging techniques to the Mg II lines in AR Lacertae to produce maps that show the location, sizes, and brightness of its plages.

Several studies using UV spectral imaging techniques appear in the literature (see, for example, Walter 1995; Neff 1995 and references therein). While the AR Lacertae results were extremely useful in locating large active regions on the stellar surface, they relied on low-resolution, low-S/N *IUE* observations of the chromospheric Mg II emission lines.

[1] Based on observations with the NASA/ESA *Hubble Space Telescope* obtained at the Space Telescope Science Institute, which is operated by the Association of Universities for Research in Astronomy, Incorporated, under NASA contract NAS5-26555.

[2] Guest Investigator with the *International Ultraviolet Explorer* satellite, which is sponsored and operated by the National Aeronautics and Space Administration, by the Science Research Council of the United Kingdom, and by the European Space Agency.

With its ability to obtain very high resolution and high S/N spectra, the GHRS on *Hubble Space Telescope* (*HST*) offers an excellent opportunity to expand upon this previous work. Furthermore, to fully understand the complexities of magnetic dynamos, different systems should be studied using multiwavelength spectral imaging. In an effort to probe several lines simultaneously with the Mg II lines, we observed the RS CVn system V711 Tau (HR 1099 = HD 22468) with the GHRS in 1993 September. While the limited phase coverage we obtained with GHRS is inadequate for detailed surface mapping, we are able to study in more detail the variability of emission lines formed over the wide temperature range characterizing the chromosphere and transition region. Simultaneous *IUE* and *Extreme-Ultraviolet Explorer* (*EUVE*) observations were obtained to provide more complete phase coverage but at lower sensitivity and spectral resolution.

V711 Tau is a short-period ($P_{rot} = 2^d.8$) RS CVn binary (G5 IV+K1 IV) that is a luminous X-ray, microwave, and UV emission source (Walter, Charles, & Bowyer 1978; Gibson, Hjellming, & Owen 1975; Simon & Linsky 1980). The orbital and stellar parameters of this system are well known (Strassmeier et al. 1993). Among the brightest and most active of the RS CVn systems, V711 Tau also has the brightest Si III] and C III] emission. The visual photometric variation, with amplitude typically about 0.1 mag but which may be as large 0.22 mag, indicates the presence of large, dark spots. The presence of cool starspots was confirmed by Ramsey & Nations (1980) using observations of the TiO molecular bands. Strong magnetic fields have been detected on V711 Tau by Donati et al. (1992) using Zeeman Doppler imaging. Among the brightest RS CVn systems, V711 Tau has also been observed quite extensively by *IUE* over many years (see Dorren & Guinan 1990 and Linsky et al. 1989, and references therein).

2. OBSERVATIONS

2.1. *GHRS Observations*

Ultraviolet observations were obtained with the GHRS on the *HST* over a 1 week interval beginning on 1993 September 14. The observing campaign, which combined both GTO and GO observations, had three primary objectives. First, hydrogen Lyα spectra were obtained at both orbital quadrature phases to measure the interstellar deuterium-to-hydrogen ratio. Results from this analysis are presented in Piskunov et al. (1996). Second, a comprehensive set of high S/N observations covering a large number of spectral features at a single phase were obtained for a detailed atmospheric analysis. These results are presented in Wood et al. (1996). Finally, in order to study chromospheric inhomogeneities, we had planned to obtain spectra of the Mg II *h* (2803 Å) and *k* (2795 Å) lines, C IV 1548 and 1550 Å, and the density-sensitive intersystem C III] 1909 Å and Si III] 1892 Å lines at eight evenly distributed phases. Unfortunately, the *HST* servicing mission in 1993 December interrupted these observations after only half were scheduled. In this paper, we present the results based on 15 spectra of various lines obtained at five unique orbital phases.

A summary of the observations for all three programs is given in Table 1. Orbital phases were computed using the ephemeris of HJD 2,442,766.080+2.83774E (Strassmeier et al. 1993). All observations were obtained with side 2 of the GHRS in ACCUM mode using the G160M, G200M, and Echelle-B gratings. See Wahlgren et al. (1991), Brandt et al. (1994), and Heap et al. (1995) for a detailed description of the GHRS prior to the installation of COSTAR. Both the small science aperture (SSA) and the large science aperture (LSA) were utilized. The spectral resolutions, defined by measuring the FWHM of several wavelength calibration emission lines, were about 0.02 Å for the Si III] and C III] SSA spectra, 0.04 Å for the Mg II region, and 0.07 Å for the C IV data in the SSA, respectively. A resolution of approximately 0.08 Å was achieved for the LSA observations of the Si III]–C III] region. The signal-to-noise ratio per diode ranged from 5:1 for the weak C III] line to 45:1 for the Mg II spectra. To ensure accurate wavelengths, calibration spectra using a Pt–Ne lamp were obtained just before or after the science spectra. The GHRS SPYBAL positioning observation (Soderblom, Sherbert, & Hulbert 1993) was used for the phase 1.22 observation of Si III], and no wavelength

TABLE 1

SUMMARY OF GHRS OBSERVATIONS

Grating	Aperture	Central Wavelength (Å)	Date	UT Start	Exposure Time (s)	HJD (+2,440,000)	Orbital Phase
G160M.....	SSA	1224	1993 Sep 14	18:50:33	3916	9245.3078	0.24
G160M.....	SSA	1549	1993 Sep 15	01:18:58	544	9245.5580	0.32
Echelle-B.....	LSA	2800	1993 Sep 15	02:35:23	108	9245.6085	0.34
Echelle-B.....	LSA	1909	1993 Sep 15	02:42:53	1197	9245.6200	0.35
Echelle-B.....	LSA	1892	1993 Sep 15	03:08:29	1197	9245.6378	0.35
Echelle-B.....	LSA	1909	1993 Sep 17	13:57:47	1197	9248.0887	1.22
Echelle-B.....	LSA	1892	1993 Sep 17	14:29:11	1197	9248.1105	1.22
G160M.....	SSA	1549	1993 Sep 18	14:26:34	544	9249.1049	1.57
Echelle-B.....	LSA	2800	1993 Sep 18	15:49:52	108	9249.1603	1.59
Echelle-B.....	LSA	1909	1993 Sep 18	15:57:22	1197	9249.1718	1.60
Echelle-B.....	LSA	1892	1993 Sep 18	16:22:58	1197	9249.1895	1.60
G200M.....	LSA	1900	1993 Sep 18	19:19:13	489	9249.3078	1.64
G160M.....	LSA	1655	1993 Sep 18	19:32:25	707	9249.3183	1.65
G160M.....	LSA	1550	1993 Sep 18	20:35:50	816	9249.3629	1.66
G160M.....	LSA	1402	1993 Sep 18	20:53:11	1197	9249.3772	1.67
Echelle-B.....	SSA	2600	1993 Sep 19	01:18:15	979	9249.5600	1.73
G160M.....	SSA	1549	1993 Sep 19	16:09:15	544	9250.1762	1.95
Echelle-B.....	LSA	2800	1993 Sep 19	17:43:58	108	9250.2395	1.97
Echelle-B.....	LSA	1909	1993 Sep 19	17:51:28	1197	9250.2510	1.98
Echelle-B.....	LSA	1892	1993 Sep 19	19:07:22	1197	9250.3037	2.00
Echelle-B.....	LSA	2800	1993 Sep 21	21:04:47	1414	9252.3865	2.73

TABLE 2

SUMMARY OF *IUE* OBSERVATIONS

Image	Date	UT (start)	HJD	Orbital Phase	Duration (s)
SWP 48645.....	1993 Sep 16	07:45:20	2,449,246.823	0.77	2100
LWP 26368.....	1993 Sep 16	08:37:55	2,449,246.860	0.78	900
SWP 48646.....	1993 Sep 16	09:08:55	2,449,246.881	0.79	2100
LWP 26369.....	1993 Sep 16	10:05:24	2,449,246.920	0.80	900
SWP 48647.....	1993 Sep 16	10:40:54	2,449,246.945	0.81	2100
LWP 26370.....	1993 Sep 16	11:36:36	2,449,246.984	0.83	600
SWP 48648.....	1993 Sep 16	12:08:59	2,449,247.006	0.83	2100
LWP 26371.....	1993 Sep 16	13:07:23	2,449,247.047	0.85	900
SWP 48649.....	1993 Sep 16	13:42:24	2,449,247.071	0.86	2100
LWP 26372.....	1993 Sep 16	14:29:54	2,449,247.104	0.87	900
LWP 26373.....	1993 Sep 16	23:49:56	2,449,247.493	0.01	900
SWP 48651.....	1993 Sep 17	00:16:05	2,449,247.511	0.01	2100
LWP 26374.....	1993 Sep 17	01:09:45	2,449,247.548	0.02	900
SWP 48652.....	1993 Sep 17	01:44:39	2,449,247.573	0.03	2100
LWP 26375.....	1993 Sep 17	02:26:54	2,449,247.602	0.04	900
SWP 48653.....	1993 Sep 17	02:58:18	2,449,247.624	0.05	2100
LWP 26376.....	1993 Sep 17	03:39:19	2,449,247.652	0.06	900
SWP 48654.....	1993 Sep 17	04:08:59	2,449,247.673	0.07	2100
LWP 26377.....	1993 Sep 17	04:48:51	2,449,247.701	0.08	900
SWP 48655.....	1993 Sep 17	05:19:02	2,449,247.722	0.09	900
LWP 26378.....	1993 Sep 17	05:51:22	2,449,247.744	0.09	900
SWP 48656.....	1993 Sep 17	06:21:03	2,449,247.765	0.10	900
LWP 26379.....	1993 Sep 17	06:53:06	2,449,247.787	0.11	900
SWP 48657.....	1993 Sep 17	07:22:26	2,449,247.807	0.12	720
LWP 26380.....	1993 Sep 17	07:59:05	2,449,247.833	0.12	900
SWP 48658.....	1993 Sep 17	08:27:58	2,449,247.853	0.13	600
LWP 26381.....	1993 Sep 17	09:01:17	2,449,247.876	0.14	600
SWP 48659.....	1993 Sep 17	09:29:54	2,449,247.896	0.15	480
LWP 26382.....	1993 Sep 17	10:02:56	2,449,247.919	0.16	480
SWP 48660.....	1993 Sep 17	10:32:14	2,449,247.939	0.16	480
LWP 26383.....	1993 Sep 17	11:04:19	2,449,247.961	0.17	420
SWP 48661.....	1993 Sep 17	11:36:10	2,449,247.983	0.18	480
LWP 26384.....	1993 Sep 17	12:08:28	2,449,248.006	0.19	480
SWP 48662.....	1993 Sep 17	12:36:53	2,449,248.026	0.19	480
LWP 26385.....	1993 Sep 17	13:10:28	2,449,248.049	0.20	600
SWP 48663.....	1993 Sep 17	13:39:55	2,449,248.069	0.21	600
LWP 26386.....	1993 Sep 17	14:12:36	2,449,248.092	0.22	720
LWP 26392.....	1993 Sep 18	01:33:08	2,449,248.565	0.38	720
SWP 48667.....	1993 Sep 18	02:07:20	2,449,248.588	0.39	1200
LWP 26393.....	1993 Sep 18	02:41:38	2,449,248.612	0.40	720
SWP 48668.....	1993 Sep 18	03:12:52	2,449,248.634	0.41	1800
LWP 26394.....	1993 Sep 18	03:50:06	2,449,248.660	0.42	720
SWP 48669.....	1993 Sep 18	04:20:44	2,449,248.681	0.42	1800
LWP 26395.....	1993 Sep 18	04:57:31	2,449,248.707	0.43	720
SWP 48670.....	1993 Sep 18	05:38:20	2,449,248.735	0.44	1800
LWP 26396.....	1993 Sep 18	06:17:12	2,449,248.762	0.45	720
SWP 48671.....	1993 Sep 18	06:47:05	2,449,248.783	0.46	1800
LWP 26397.....	1993 Sep 18	07:25:30	2,449,248.809	0.47	720
SWP 48672.....	1993 Sep 18	07:56:23	2,449,248.831	0.48	1800
LWP 26398.....	1993 Sep 18	08:34:17	2,449,248.857	0.49	720
SWP 48673.....	1993 Sep 18	09:06:17	2,449,248.879	0.49	900
LWP 26399.....	1993 Sep 18	09:40:51	2,449,248.903	0.50	480
SWP 48674.....	1993 Sep 18	10:11:31	2,449,248.925	0.51	900
LWP 26400.....	1993 Sep 18	10:45:50	2,449,248.948	0.52	480
SWP 48675.....	1993 Sep 18	11:24:38	2,449,248.975	0.53	600
LWP 26401.....	1993 Sep 18	11:59:28	2,449,249.000	0.54	480
SWP 48676.....	1993 Sep 18	12:32:58	2,449,249.023	0.54	1800
LWP 26402.....	1993 Sep 18	13:18:14	2,449,249.054	0.56	720
SWP 48677.....	1993 Sep 18	13:53:47	2,449,249.079	0.56	1800
LWP 26403.....	1993 Sep 18	14:30:39	2,449,249.105	0.57	720
LWP 26406.....	1993 Sep 18	23:49:20	2,449,249.493	0.71	900
SWP 48682.....	1993 Sep 19	00:13:07	2,449,249.509	0.72	1800
LWP 26407.....	1993 Sep 19	00:57:33	2,449,249.540	0.73	900
SWP 48683.....	1993 Sep 19	01:26:36	2,449,249.560	0.73	1800
LWP 26408.....	1993 Sep 19	02:02:42	2,449,249.585	0.74	900
SWP 48684.....	1993 Sep 19	02:29:34	2,449,249.604	0.75	1800
LWP 26409.....	1993 Sep 19	03:05:52	2,449,249.629	0.76	600
SWP 48685.....	1993 Sep 19	03:34:15	2,449,249.649	0.77	600
LWP 26410.....	1993 Sep 19	04:06:21	2,449,249.671	0.77	600
SWP 48686.....	1993 Sep 19	04:34:10	2,449,249.690	0.78	480
LWP 26411.....	1993 Sep 19	05:06:09	2,449,249.713	0.79	600

TABLE 3

APT PHOTOMETRY[a]

HJD (+2,440,000)	Orbital Phase	ΔU	ΔB	ΔV
9233.9633.....	0.24	2.305 ± 0.006	1.891 ± 0.003	1.560 ± 0.002
9236.9616.....	0.29	2.288 ± 0.006	1.905 ± 0.003	1.575 ± 0.001
9237.9132.....	0.63	...	1.948 ± 0.017	1.618 ± 0.018
9238.9060.....	0.98	2.269 ± 0.007	1.883 ± 0.006	1.560 ± 0.002
9239.9043.....	0.33	2.295 ± 0.001	1.912 ± 0.004	1.597 ± 0.008
9240.9781.....	0.71	2.331 ± 0.004	1.916 ± 0.003	1.592 ± 0.004
9241.9502.....	0.05	2.290 ± 0.003	1.883 ± 0.002	1.560 ± 0.006
9246.9517.....	0.82	2.294 ± 0.004	1.894 ± 0.003	1.564 ± 0.003
9248.8837.....	0.50	2.382 ± 0.010	1.983 ± 0.006	1.642 ± 0.005
9249.8883.....	0.85	2.264 ± 0.006	1.889 ± 0.003	1.556 ± 0.001
9250.9348.....	0.22	2.291 ± 0.001	1.885 ± 0.002	1.551 ± 0.006
9251.8820.....	0.55	2.360 ± 0.005	1.965 ± 0.003	1.640 ± 0.006
9252.9251.....	0.92	2.281 ± 0.008	1.889 ± 0.004	1.547 ± 0.003
9253.8771.....	0.26	2.300 ± 0.005	1.892 ± 0.005	1.579 ± 0.004
9256.0033.....	0.01	2.282 ± 0.002	1.872 ± 0.004	1.552 ± 0.002
9256.8607.....	0.31	2.334 ± 0.001	1.927 ± 0.003	1.591 ± 0.003
9257.8541.....	0.66	2.335 ± 0.002	1.920 ± 0.003	1.604 ± 0.004
9257.9884.....	0.70	2.293 ± 0.005	1.903 ± 0.009	1.586 ± 0.004
9258.8943.....	0.02	2.275 ± 0.005	1.874 ± 0.001	1.554 ± 0.003
9259.8647.....	0.37	2.351 ± 0.003	1.944 ± 0.001	1.616 ± 0.006
9261.8893.....	0.08	2.292 ± 0.010	1.876 ± 0.004	1.552 ± 0.005
9262.8447.....	0.42	2.363 ± 0.008	1.957 ± 0.003	1.636 ± 0.002
9263.0220.....	0.48	2.388 ± 0.020	1.980 ± 0.007	1.638 ± 0.003
9263.8461.....	0.77	2.297 ± 0.005	1.888 ± 0.002	1.560 ± 0.002
9263.9894.....	0.82	2.295 ± 0.004	1.873 ± 0.001	1.549 ± 0.003
9268.9260.....	0.56	2.368 ± 0.007	1.967 ± 0.009	1.629 ± 0.007

[a] Comparison star was HD 22484 ($V = 4.28$; $U-B = 0.08$; $B-V = 0.58$).

calibration was obtained with the LSA C IV spectrum. Previous studies have found that the default wavelength calibration is accurate to better than 1 km s^{-1} for the first-order gratings and 0.6 km s^{-1} for the Echelle-B grating. Using the calibration spectra taken at the time of the science observation improves the accuracy to approximately 0.1 km s^{-1}. Using the SPYBAL spectrum yields an accuracy somewhere in between the default calibration and that obtained with a contemporaneous comparison observation.

All observations were calibrated using the GHRS Data Analysis Facility software current as of 1993 December (Blackwell et al. 1993). The GHRS flux calibration is accurate to about 10%, and prior to COSTAR the repeatability of flux measurements is usually better than 1% in the LSA. Line fluxes and profile models for the emission lines were calculated with the ICUR fitting code based on Bevington's (1969) CURFIT (Neff 1987; Neff et al. 1989) using least-squares Gaussian fits. A quadratic was used to fit the background. In most cases a single Gaussian was used to model the emission lines, but this is described in greater detail below. Our method of line fitting is essentially identical to that used by Wood et al. (1996), but the two sets of measurements were carried out independently.

2.2. *IUE Observations*

Observations with *IUE* were obtained nearly continuously starting on 1993 September 16 and covering one complete orbital period of V711 Tau. Both SWP and LWP spectra were taken. Details of the observations are found in Table 2. Spectra were extracted from the *IUE* images and calibrated using the RDAF package of IDL routines. No correction for camera degradation was made to the data. As with the *HST* data, fluxes were measured using ICUR, but only a single Gaussian was used to fit each line.

2.3. *EUVE Photometry*

HR 1099 was observed by *EUVE* over the period 1993 September 16–22, contemporaneously with the majority of our GHRS observations. Thus, the coronal conditions during these observations are known. The Deep Survey (DS) photometric signal is measured through a Lexan boron filter whose effective area peaks at 90 Å with a bandpass of 40–190 Å. In the case of HR 1099, the DS signal is dominated by hot coronal emission lines formed at temperatures of $\sim 10^7$ K. The DS counts have been binned into roughly 10 minute intervals and the count rate derived using accurate timing information for the selected intervals. The source counts are extracted from a circle with radius 2′ centered on HR 1099, while the background signal is determined from an annulus with inner and outer radii of 4′ and 6′. The timing bins were checked for accurate detector on and off times. Bins that showed high background count rates were excluded, and this results in several significant gaps in coverage when the satellite was able to observe HR 1099 only while it was close to the high backgrounds produced by the South Atlantic Anomaly, the auroral zones, and daytime observing conditions.

2.4. *APT Observations*

The *UBV* data presented in this paper were collected by the Phoenix 25 cm Automated Photometric Telescope (APT). The telescope feeds a single-channel photometer equipped with an uncooled 1P21 photomultiplier and standard filters matching the Johnson *UBV* system. HD 22484 and HD 22796 were chosen as comparison and check stars, respectively. The observations were corrected for atmospheric extinction and transformed to the *UBV* system. The typical errors of the differential *UBV* photometry are of the order of 0.006, 0.004, and 0.004 mag, respectively. These data are listed in Table 3. All values include the visual

companion ADS 2644B. Additional details on the procedure of observations are given by Rodonò & Cutispoto (1992).

3. RESULTS

3.1. *Interstellar* Mg II *Lines*

An echelle spectrum of the Mg II *h* and *k* lines is shown in Figure 1. Preliminary fitting of the GHRS data and previous *IUE* results (Linsky et al. 1989) show that the Mg II line profiles could be characterized by at least two emission components, one each for the G and K star, and an interstellar absorption feature. Radial velocities for the two emission features roughly follow the expected orbital velocities of the two stars.

V711 Tau is located 36 pc away in a direction of the local interstellar medium that is known to have a particularly low column density (Murthy et al. 1987). The Crutcher (1982) formula predicts a relative redshift for the interstellar material in this line of sight of $+22.6$ km s^{-1} (0.21 Å). Whereas the interstellar (IS) absorption is weak and unresolved in all *IUE* spectra, in our GHRS spectra it is resolved into at least three discrete components. The model

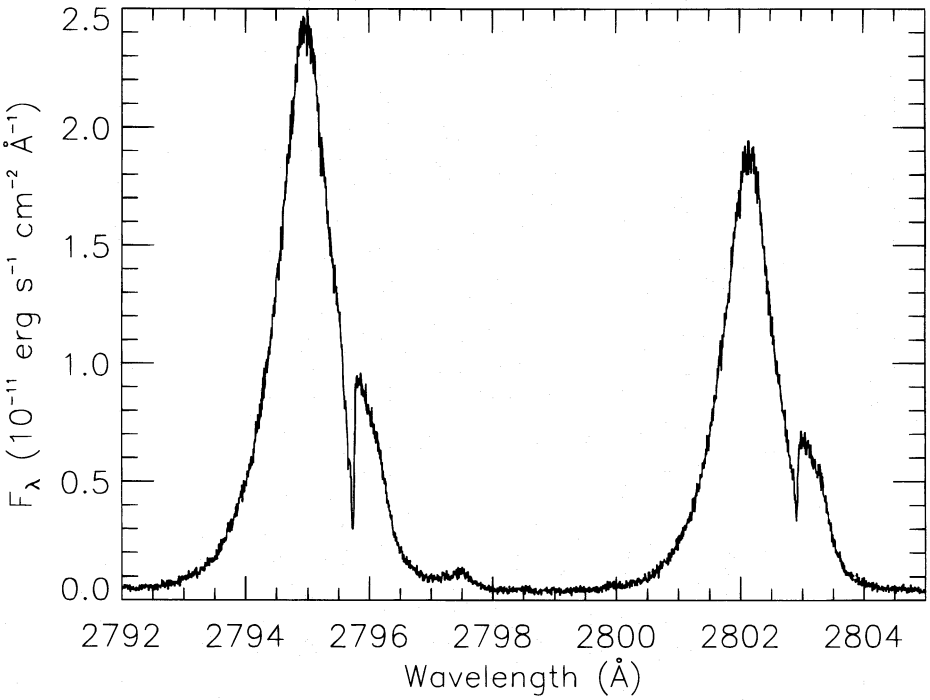

FIG. 1.—The observed GHRS spectra of the Mg II *k* (2795.53 Å) and *h* (2802.70 Å) lines at phase 2.73. The broad lines are due to chromospheric emission primarily from the K star in V711 Tau, and the sharp absorption features are due to the local interstellar medium.

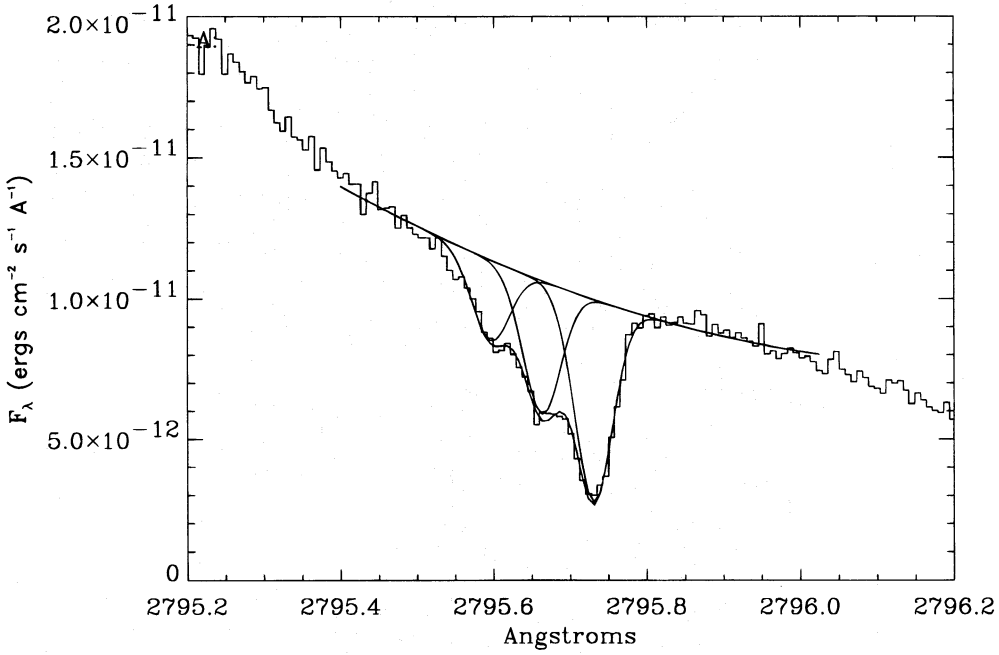

FIG. 2.—The interstellar Mg II *k* line at phase 2.73 fitted with three Gaussian components of fixed width but variable strength and position

shown in Figure 2 includes three components with a fixed width of 0.06 Å (equivalent $v \sin i = 5.6$ km s^{-1}) but variable position and line depth. The measured line positions correspond to velocities of +7.3, +14.5, and +21.7 km s^{-1}, and the corresponding equivalent widths are 0.01, 0.03, and 0.04 Å. These IS features are analyzed by Piskunov et al. (1996).

The 2798 Å emission line of Mg II can also be detected. Since we can fit only five Gaussian components at a time using the current version of ICUR, the multiple IS features, the background, and the 2798 Å emission line were fitted and then subtracted from the data before modeling the chromospheric lines.

3.2. *Chromospheric* Mg II *h and k Lines*

The Mg II emission features from the two stars in V711 Tau are blended together. Of our four Mg II spectra, the data from phase 2.73 represent the greatest radial velocity separation between the two components. Therefore, we used this phase to estimate the relative contributions to the emission line from each star, which was then used as a starting point in the modeling for the other phases. In our initial approach, we used the best two-component model derived from the phase 2.73 observation to fit the other phases. The stronger emission component lies closest to the expected radial velocity for the K star. The line widths and fluxes were then frozen to their phase 2.73 values, while the central wavelengths were allowed to vary in order to match the orbital motion of the stars. The residuals between these "two-component" fits and the observed spectra are shown in Figure 3. Model parameters and residual fluxes are listed in Table 4. It is clear that two components do not adequately fit the profiles, especially in the line wings. These broad wings are roughly symmetric about the K-star position. We attempted several variations on the two-component models (i.e., allowing certain parameters to vary from their phase 2.73 value), but the results were very similar.

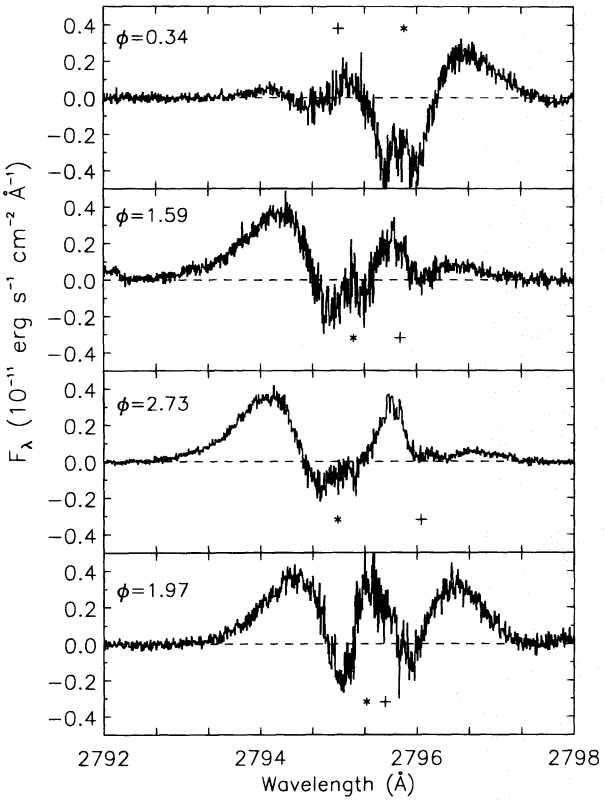

FIG. 3.—Residuals of the Mg II *k* after subtracting 2 Gaussians, one each for the K and G star. The asterisk and plus symbols indicate the predicted orbital position of the K and G star, respectively. The subtraction of the interstellar medium components introduces some additional error between 2795.5 and 2795.8 Å.

TABLE 4

MG II TWO-COMPONENT FIT SUMMARY

ORBITAL PHASE	RESIDUAL FLUX[b]	K STAR		G STAR	
		λ (Å)	Δ[c]	λ (Å)	Δ[c]
		k Line[a]...			
0.34.....	−2.2	2794.894	−0.6	2795.779	−0.1
1.59.....	41.6	2795.792	−3.3	2795.109	−3.3
2.73.....	42.2	2795.957	2.5	2794.953	2.5
1.97.....	60.4	2795.884	2.2	2795.320	2.2
		h Line[d]...			
0.34.....	−1.4	2802.093	2.5	2802.951	1.2
1.59.....	23.8	2802.943	8.9	2802.258	−5.6
2.73.....	23.1	2803.091	−4.2	2802.106	0.6
1.97.....	32.8	2802.916	27.4	2802.484	1.5

[a] The two-components used the following parameters: $\text{flux}_G = 49.4 \times 10^{-13}$ ergs s^{-1} cm^{-2}, $\text{flux}_K = 231 \times 10^{-13}$ ergs s^{-1} cm^{-2}, $v \sin i_G = 74$ km s^{-1} (0.69 Å) and $v \sin i_K = 95$ km s^{-1} (0.88 Å).

[b] Residual flux, in units of 10^{-13} ergs s^{-1} cm^{-2}.

[c] Δ is the difference in km s^{-1} between the measured central velocity of the line and that expected from the orbital solution.

[d] The two-components used the following parameters: $\text{flux}_G = 38.6 \times 10^{-13}$ ergs s^{-1} cm^{-2}, $\text{flux}_K = 172 \times 10^{-13}$ ergs s^{-1} cm^{-2}, $v \sin i_G = 72$ km s^{-1} (0.67 Å) and $v \sin i_K = 94$ km s^{-1} (0.88 Å).

In attempt to better account for the non-Gaussian wing emission, we tried replacing the Gaussian model with a Voigt profile. This representation did considerably poorer in fitting the lines than did the Gaussian profile, as the Voigt profile was too narrow in the line core. Although our observations were taken prior to the installation of COSTAR, the wings are far too broad to be explained by the telescope's aberration of the point-spread function. Similar broad wings have been observed in GHRS spectra of the transition region lines of Capella and AU Mic (Linsky et al. 1995; Linsky & Wood 1994).

Rodonò et al. (1987) reported broad, non-Gaussian wings in the *IUE* spectra of V711 Tau obtained in 1983 October. With relatively low S/N spectra obtained at only four phases, they were unable to determine if these wings were related to discrete regions on the stellar surface, high-speed flows, or were simply an artifact of assuming a Gaussian-shaped profile.

Wood et al. (1996) fitted the phase 2.73 Mg II profile by adding a third, very broad Gaussian. They proposed that the broad component is a manifestation of continuous, low-level flaring. When fitting the wings using a broad Gaussian, the flux of the component having a width on the order of $v \sin i$ and representing the global stellar emission is drastically reduced. In fact, in these simple three-component models, the broad component accounts for the *majority* of the Mg II line flux.

For comparison with the Wood et al. (1996) results, we have fitted a similar three-Gaussian model to *all four* of the Mg II spectra. Since the broad residual flux is roughly symmetric about the narrow K star component, we assumed that the broad feature is associated with the K star. Hence-

forth, we will refer to the narrow global K and G star components as K_N and G_N, respectively, while the broad feature will be designated as K_B. We constrained the positions of the global K- and G-star components to be within a few km s^{-1} of the predicted values, and we used the three Gaussian parameters derived from the fit to the phase 2.73 spectrum as a starting point in modeling the spectra at the other 3 phases. As a first approximation the central wavelength of K_B was fixed to that of K_N. Acceptable fits were obtained in this manner for three of the four phases, the exception being phase 1.97, near orbital conjunction. No acceptable fit using the above scheme could be obtained unless we added an additional component or allowed the central wavelength of K_B to vary. A marginally acceptable fit was achieved by redshifting K_B from the predicted orbital velocity by 5–12 km s^{-1}.

Final three-component fits for both lines are shown in Figure 4, with the model parameters listed in Table 5. These fits are similar to those of Wood et al. (1996) in that the majority of the flux is in the broad component. We attempted to minimize the flux in the broad component but could not successfully fit the line profile. A more complex assumed intrinsic profile (due to a nonuniform distribution of active regions on the stellar surface) could combine with a much weaker broad component to reproduce the observed profile, but spectra obtained with higher S/N and much better phase coverage would be required to constrain any model more complex than our three-component fits.

Fluxes and line widths from the *IUE* LWP spectra were measured for the Mg II *h* and *k* lines. At the spectral resolution and S/N of the *IUE* spectra, single-Gaussian fits provide an adequate measure of the total line flux. The parameters for the *IUE* Mg II line fits are listed in Table 6, and the fluxes are plotted in Figure 5.

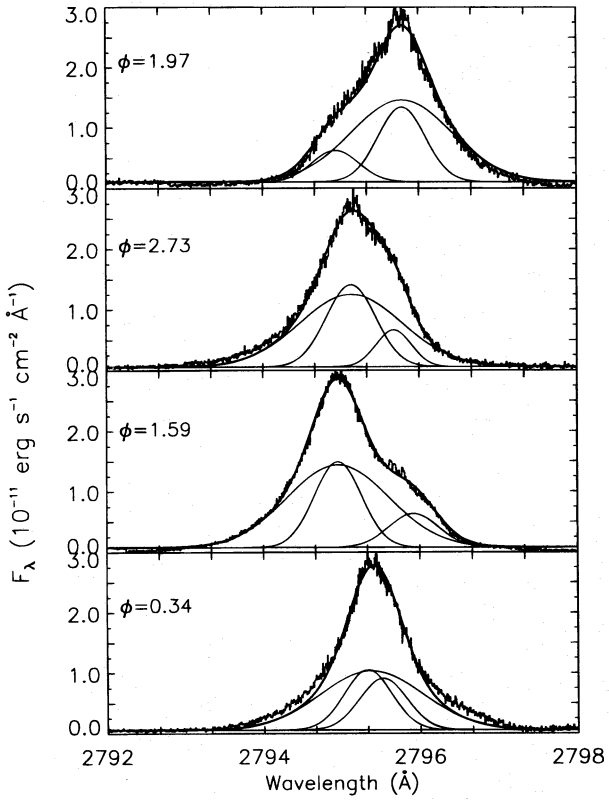

FIG. 4.—Final three-component model fits for the Mg II *k* line at thefour phases. Note that K_B and K_N are not at the same velocity at phase 1.97 and that the fit is still poor in the line wings.

TABLE 5

MG II THREE-COMPONENT FIT SUMMARY

	WIDTH[a]			FLUX[b]			ΔRV[c]	
PHASE	K_N	K_B	G	K_N	K_B	G	K_N	G
k Line:								
0.34	0.71	1.51	0.70	75.0	174.2	32.7	0.2	3.6
1.59	0.73	1.55	0.75	91.9	180.3	40.0	−1.2	−2.5
1.97	0.71	1.55	0.88	67.2	167.4	87.2	2.9/4.7[d]	2.2
2.73	0.71	1.53	0.74	87.7	181.9	36.3	2.5	−4.5
Mean...	0.71	1.54	0.77	80.4	176.0	49.0	1.1	−0.3
σ.....	0.01	0.02	0.08	11.4	6.6	25.6	1.9	3.8
h Line:								
0.34	0.69	1.39	0.70	61.5	116.0	27.1	1.8	4.9
1.59	0.59	1.48	0.52	60.6	146.8	15.2	−0.6	−1.0
1.97	0.63	1.48	0.60	57.4	147.3	29.4	2.4/11.7[d]	4.0
2.73	0.66	1.53	0.58	67.9	139.2	20.3	2.7	3.7
Mean...	0.64	1.47	0.60	61.8	137.3	23.0	1.6	2.9
σ.....	0.04	0.06	0.07	4.4	14.7	6.5	1.5	2.7

[a] Deconvolved FWHM in angstroms.
[b] Fluxes are in units of 10^{-13} ergs s^{-1} cm^{-2}.
[c] ΔRV is the difference in km s^{-1} between the measured central velocity of the line and that expected from the orbital solution.
[d] The second number represents the shift of the broad component.

The DS light curve (Fig. 6) and the *IUE* observations (Fig. 5) show that HR 1099 underwent two large flare events during the observation starting at roughly September 17.2 and September 19.2. The decay of both flares lasted over half a day. There was significant low-level flaring on September 20, which is seen superimposed on the decay of the large September 19 flare. The timing of the GHRS spectra is also shown on Figure 6. The observations on September 17 ($\phi = 1.22$) lie on the decay phase of the first large *EUVE* flare, those on September 18 ($\phi = 1.57$–1.73) appear to be during an interval of coronal quiescence, and those later on September 19 ($\phi = 1.95$–2.00) were obtained during a period of extended low-level flaring on the decay of the second *EUVE* flare. Contemporaneous VLA and AT radio continuum observations (Jones et al. 1996) show a similar pattern of coronal flaring. However, the radio coverage begins on September 14 and shows even larger radio flaring (up to 0.35 Jy at 3 and 6 cm) at the time of the September 14–15 GHRS observations.

The extra phase coverage provided by the *EUVE* and *IUE* data reveals that V711 Tau was undergoing a major episode of flaring activity in 1993 September. Nearly continuous flaring for more than a 24 hr period (peaking around phase 1.1) is reminiscent of the radio outburst in 1978 February that led to a series of papers in the Astronomical Journal (Vol. 83 [1978 December]), and it is by far the most long-lived and energetic chromospheric and transition region flare ever observed (Neff 1991; see Kürster & Schmitt 1996 for a discussion of a longer duration coronal event). The total excess energy radiated in the far-ultraviolet lines alone (not including Lyα) during the 1993 September flare was 5×10^{35} ergs, and the integrated luminosity in these lines at flare peak was 2.1×10^{31} ergs s^{-1}. The flare that occurred around phase 1.77 reached an even higher luminosity. A third, short-lived flare was seen in the transition region lines at phase 1.51. The UV flares are strongest right at the start of the EUV and high-frequency radio flares (Jones et al. 1996). The flares as observed by *IUE* will be discussed in greater detail by Neff et al. (1996).

TABLE 6

IUE LWP Mg II MEASUREMENTS

LWP	Phase	Flux[a]	Wavelength	FWHM	Flux[a]	Wavelength	FWHM
26368.....	0.782	223.65	2795.109	1.167	174.62	2802.286	1.179
26369.....	0.803	227.10	2795.118	1.493	138.06	2802.189	0.921
26370.....	0.826	205.96	2795.146	1.155	161.74	2802.353	1.106
26371.....	0.848	249.11	2795.300	1.157	167.44	2802.478	1.064
26372.....	0.868	245.69	2795.323	1.112	178.74	2802.526	1.069
26373.....	1.005	247.47	2795.514	1.019	192.21	2802.695	0.937
26374.....	1.025	257.92	2795.578	1.149	192.60	2802.762	0.949
26375.....	1.043	310.03	2795.695	1.297	220.81	2802.857	1.184
26376.....	1.061	349.45	2795.694	1.409	244.40	2802.873	1.267
26377.....	1.078	388.51	2795.755	1.541	292.46	2802.923	1.372
26378.....	1.094	347.62	2795.833	1.402	264.39	2802.026	1.281
26379.....	1.109	343.34	2795.875	1.380	250.05	2802.050	1.169
26380.....	1.125	351.04	2795.913	1.433	250.79	2803.093	1.182
26381.....	1.140	374.07	2796.016	1.458	218.32	2803.142	1.178
26382.....	1.155	396.47	2795.985	1.741	262.92	2803.007	1.241
26383.....	1.170	356.38	2796.080	1.648	206.65	2803.173	1.194
26384.....	1.186	356.00	2796.087	1.622	232.11	2803.206	1.357
26385.....	1.201	326.67	2796.103	1.651	223.30	2803.245	1.441
26386.....	1.216	338.53	2796.101	1.691	217.48	2803.280	1.463
26392.....	1.383	270.17	2795.729	1.413	184.29	2802.907	1.209
26393.....	1.399	252.01	2975.697	1.320	180.74	2802.867	1.194
26394.....	1.416	250.01	2975.680	1.288	177.90	2802.820	1.054
26395.....	1.433	243.42	2795.560	1.123	170.30	2802.778	1.031
26396.....	1.452	244.67	2795.567	1.043	161.05	2802.761	0.920
26397.....	1.469	228.76	2795.506	0.984	171.95	2802.701	0.960
26398.....	1.486	226.74	2795.488	0.952	148.44	2802.691	0.788
26399.....	1.502	220.10	2795.482	0.959	160.60	2802.576	0.958
26400.....	1.518	225.06	2795.451	0.904	159.99	2802.605	0.837
26401.....	1.536	233.88	2795.488	1.017	141.50	2802.722	0.849
26402.....	1.555	236.51	2795.447	1.059	168.69	2802.643	0.963
26403.....	1.573	244.45	2795.445	1.087	156.44	2802.649	0.942
26406.....	1.710	246.73	2795.045	1.214	167.26	2802.213	1.104
26407.....	1.726	256.09	2795.045	1.244	174.80	2802.252	1.218
26408.....	1.742	311.78	2795.055	1.265	212.71	2802.208	1.111
26409.....	1.758	384.91	2795.026	1.310	253.90	2802.209	1.135
26410.....	1.773	394.04	2795.091	1.294	267.72	2802.287	1.073
26411.....	1.787	409.68	2795.138	1.369	270.82	2802.313	1.218

[a] Fluxes are in units of 10^{-13} ergs s^{-1} cm^{-2}.

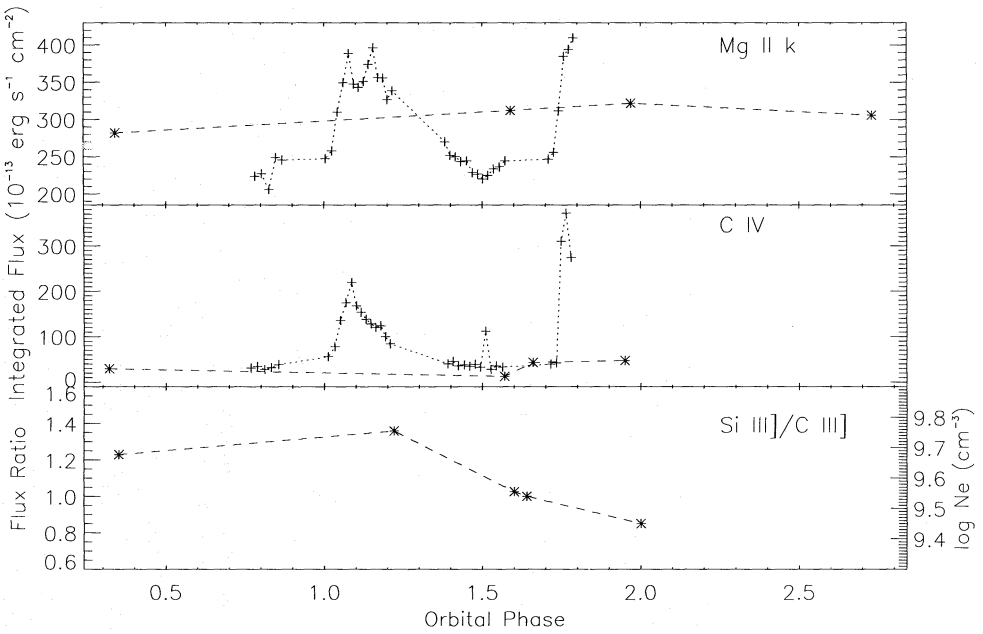

FIG. 5.—Total integrated line fluxes from *IUE* (*dotted lines*) and *HST* (*dashed lines*). The *IUE* data were obtained with nearly complete coverage for a single orbital cycle, whereas the *HST* data have sparse phase coverage and were taken over two orbits. The top panel shows the Mg II *k* flux, and the middle panel shows the integrated C IV flux (from both lines in the doublet). In the bottom panel we show the ratio of the Si III] and C III] line fluxes from the GHRS data only, along with an approximate density scale on the right-hand axis. The *IUE* data show that the system was undergoing a major flaring episode in 1993 September. The absolute flux calibration appears to be inconsistent for the two instruments, but none of the data were obtained strictly simultaneously.

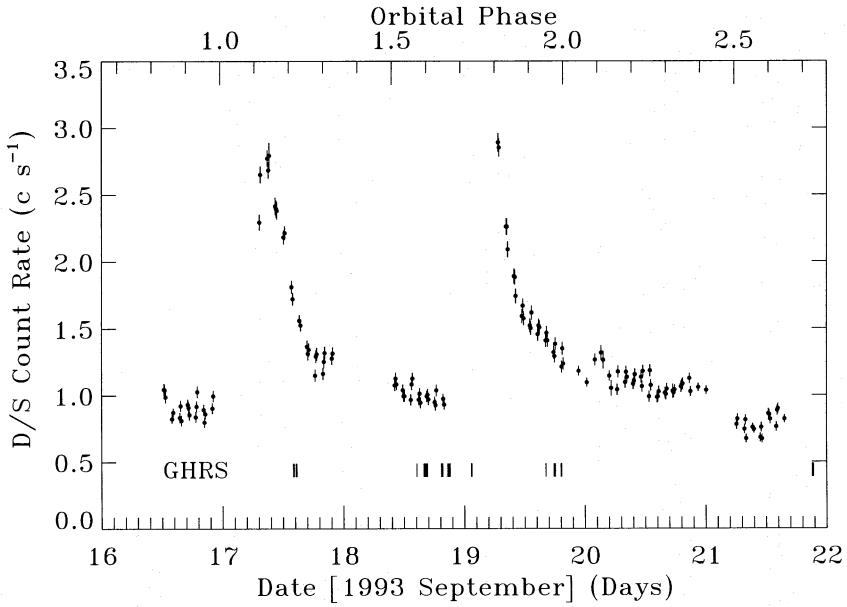

FIG. 6.—The DS photometer light curve derived from the entire *EUVE* coverage shows that HR 1099 underwent two large flare events during the observation starting at roughly September 17.2 and 19.2.

In this context, it is dangerous to interpret any of the GHRS spectra as typical of the quiescent atmosphere. Only one of the Mg II spectra was obtained close to simultaneously, and its flux level was much higher than the nearest *IUE* spectrum. The difference could be due to different calibrations of the absolute flux scales of *IUE* and *HST* or to difference in measuring technique, but most likely it could be that the data are not simultaneous with all of the *HST* Mg II spectra being obtained during flares.

3.3. *Transition Region* (C IV *and* Si IV) *Lines*

The high-resolution GHRS spectra allow us to spectrally resolve the C IV and Si IV doublets. The GHRS spectra of the C IV lines obtained at 4 phases are shown in Figure 7. For the three high-resolution but low-S/N SSA spectra, single Gaussians were adequate to represent the lines. However, broad wings are evident with high S/N in the LSA observation at phase 1.66. Since the widths of these features are much broader than expected due to the *HST* mirror aberration (see Fig. 4 in Linsky & Wood 1994), we conclude that the wings are not an artifact of the telescope point-spread function. Wood et al. (1996) conclude that the broad wing at this phase, similar to those seen in Mg II, results from microflaring on the K star.

The spectrum at phase 1.57 showed a very marked decrease in the C IV flux. Comparing the measured GHRS flux values (Table 7) both with the contemporaneous *IUE* values (Table 8) and with the historical *IUE* values (Dorren & Guinan 1990), the measured flux at this phase would be the lowest ever observed for V711 Tau. For comparison, we

TABLE 7

MEASURED GHRS LINE FLUXES

Ion	Phase	Wavelength (Å)	Flux[a]	FWHM (Å)	Wavelength (Å)	Flux[a]	FWHM (Å)
Si IV.....	1.67	1393.514	5.44	0.85	1402.499	2.61	0.85
O IV].....	1.67	1400.890	0.56	0.74	...	...	...
C IV	0.32	1548.378	20.35	0.83	1550.931	9.18	0.67
C IV	1.57	1548.017	9.11	0.85	1550.652	3.59	0.69
C IV[b]	1.66	1547.977	28.48	0.53	1550.533	14.72	0.46
C IV	1.95	1548.160	31.75	1.01	1550.720	15.51	0.88
Si III].....	0.35	1892.176	2.63	0.80	...	...	...
Si III].....	1.22	1892.463	5.23	1.01	1892.484	0.69	0.15
Si III].....	1.60	1891.707	3.25	0.91	...	...	...
Si III].....	1.64	1891.674	2.43	1.00	...	...	...
Si III].....	2.00	1892.042	3.29	0.60	...	...	...
C III].....	0.35	1908.890	2.14	0.97	...	...	...
C III].....	1.22	1909.295	3.85	1.10	...	...	...
C III].....	1.60	1908.403	3.17	1.52	...	...	...
C III].....	1.64	1908.192	2.83	1.39	...	...	...
C III].....	2.00	1908.603	3.87	1.27	...	...	...

[a] Fluxes are in units of 10^{-13} ergs s^{-1} cm^{-2}.

[b] Parameters given here are for the narrow component except for the flux, where the combined line flux is listed.

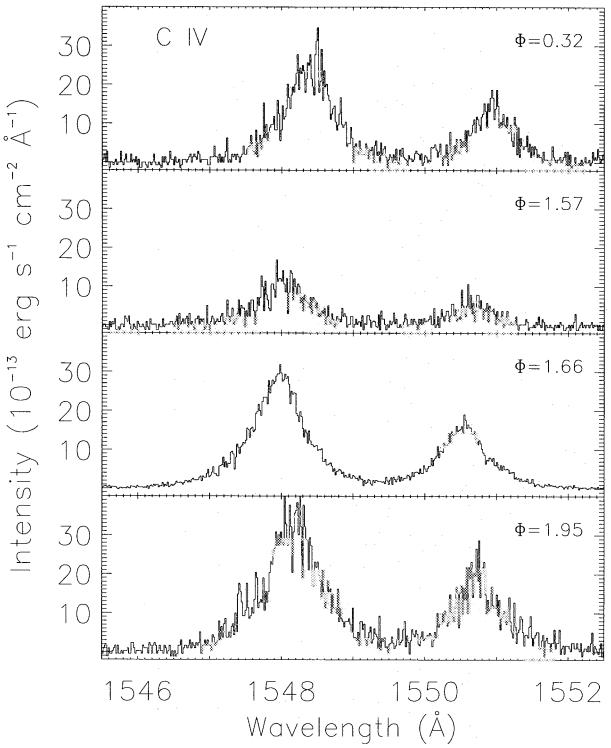

FIG. 7.—The four observed GHRS spectra of the C IV lines. The observation at phase 1.66 was obtained through the LSA. The flux drop-out at phase 1.57 is likely due to poor centering in the SSA.

plot the C IV fluxes as measured in both the 1993 September GHRS and *IUE* SWP data in Figure 5. The *IUE* data clearly show several flares during the gaps in the GHRS observations, but phase 1.57 is the only point where the two data sets overlap. There is no corresponding drop in the SWP C IV flux, suggesting something anomalous with the GHRS spectrum. One possibility is that the target was not centered in the SSA; all subsequent observations near phase 1.57 were obtained with the LSA, where centering in the aperture is less critical. The observing sequence for the three SSA observations were identical: target acquisition in the LSA followed by a peak-up in the SSA (Duncan 1992). Hulbert & Baggett (1993) note that there was a slight centering problem with the then-default 3 × 3 peak-up in the SSA using the N2 mirror, resulting in the target being slightly off center. In order to verify the success of the target acquisitions in positioning the target in the aperture, we examined the telescope's engineering telemetry. In all three cases the target was found in the same dwell-point map, No. 9 (see Hulbert & Baggett). Therefore, all of our SSA C IV data suffer some loss in throughput. Based on the overlap at phase 1.57, the SSA observations should be approximately 2.5 times larger than measured; the LSA observation at phase 1.66 should be unaffected.

Table 9 lists the measured velocity of the C IV lines relative to the orbital velocity of the K star. Velocities at three of the four phases are consistent with each other and appear to be systematically shifted toward the G star's position. Wood et al. (1996) conclude that the contribution to the C IV flux of the G star was insignificant compared to the K star, even though the G star contributes approximately 16% of the total Mg II flux. Based on the scaling relations in Ayres, Marstad, & Linsky (1981), we would expect the G star's contribution to be about 7% at C IV. As a test, we modeled the C IV 1548 Å line at phase 0.32 by including a narrow Gaussian centered on the G star position. We find that a 8% contribution to the line flux from the G star is consistent with the observed redshift, but the G star contribution could be larger. If we do not include a broad component, then the G star's contribution could be as much as 15%, but a weak (roughly a few percent), narrow feature is still required to fit the opposite line wing. We do not have any C IV spectra near quadrature that would allow us to estimate the contribution of the G star to the total C IV flux independently. A shift of 21 km s^{-1} (in the direction of the G star) was observed at phase 1.95. Since this phase shows the largest shift, we conclude that a flare, possibly on the G star, occurred at that time.

The Si IV region of the spectra is shown in Wood et al. (1996). The O IV] 1401.2 Å line is clearly separated from the 1402.8 Å Si IV line. Furthermore, the weaker O IV] lines at 1399.8 and 1404.8 Å can be observed. Since a spectrum of the Si IV region was obtained at only one phase, we cannot establish variability in the profile but the Si IV profile appears to be asymmetric. Wood et al. (1996) conclude that this Si IV profile also consists of broad component and a global emission component from the K star. As we show in Figure 8, however, the profile can be fitted equally well using a stronger broad component plus a weak narrow component. In this fit, the narrow component is blueshifted with respect to the K star by 8 km s^{-1} and the center of the stronger feature is shifted substantially toward the G star, suggesting that the G star contributes a significant proportion of the total Si IV flux. Other models can fit the profile equally well.

3.4. *Density Diagnostics*

The integrated C III] and Si III] line fluxes and the centroid velocities are listed in Tables 7 and 9. All of the C III] and Si III] profiles are displayed in Figure 9. The ratio of the flux in these two lines is sensitive to electron density, N_e. The ratio is poorly determined in the *IUE* spectra because the C III] line is weak, but it is relatively well determined from the GHRS data (see Fig. 5). We are fortunate to have obtained spectra of these density-sensitive lines in the middle of the major flaring outburst, at phase 1.22. At this phase, their ratio and therefore N_e was at its maximum.

We had planned to acquire high-quality spectra of these lines at many orbital phases. This would permit us to measure the density in the discrete regions revealed through spectral imaging with C IV line. Nevertheless, the Si III] spectrum obtained at phase 1.22, during the flare (see Fig. 9) shows a pronounced profile asymmetry, whereas it is absent or at least much less pronounced in the C III] spectrum. Thus, the narrow component of the Si III] line appears to originate largely from the high-density flaring region. Both lines were shifted substantially at this phase (Table 9). The wavelength calibration of the C III] spectrum was obtained after the actual science observation, but none was obtained for the Si III] data. We see no reason why the accuracy of the wavelength scale should depend on whether the comparison spectra were obtained before or after the science data. To verify this, we remeasured the profiles using the default wavelength calibration. We also recalibrated the data using the SPYBAL observations obtained prior to the science spectrum. In these cases, the measured redshift was even greater by 2–4 km s^{-1}. The default calibration could not be

1996ApJ...470.1172D

TABLE 8

INTEGRATED *IUE* SWP FLUXES

SWP	Phase	C III λ1176[a]	N V λ1238	O I λ1304	C II λ1335	Si IV λ1394	C IV λ1550	He II λ1640	C I+O III λ1660	Si II λ1817	Al III λ1862	Si III] λ1892	C III] λ1909
48645.....	0.769	4.87	3.68	12.98	19.95	7.96	31.32	15.51	10.29	13.51	25.68	1.76	0.73
48646.....	0.789	12.61	...[b]	14.44	21.23	13.30	34.41	18.04	13.60	22.96	1.49	...[b]	...[b]
48647.....	0.812	...[b]	...[b]	14.14	22.24	10.68	28.00	21.01	13.61	13.52	2.63	0.92	...[b]
48648.....	0.833	4.35	4.63	15.59	21.36	7.55	32.18	18.38	12.48	13.33	1.86	2.56	1.01
48649.....	0.856	6.42	5.07	14.88	22.86	8.63	38.29	18.56	12.15	14.33	3.54	1.85	1.03
48651.....	1.012	17.87	7.88	16.60	31.13	14.56	55.89	25.86	15.17	15.85	5.78	2.57	0.51
48652.....	1.033	11.67	6.27	19.24	37.46	21.57	78.11	28.22	15.86	16.13	13.60	2.76	1.78
48653.....	1.051	23.22	13.24	21.72	54.21	40.18	135.79	39.73	21.48	19.61	15.34	4.20	2.07
48654.....	1.068	50.86	20.55	40.52	88.21	89.94	174.58	57.37	27.42	29.57	43.01	8.58	...[b]
48655.....	1.086	25.51	10.53	24.33	64.58	42.26	219.56	60.23	25.74	25.48	19.08	5.80	5.98
48656.....	1.101	13.90	10.79	20.53	48.93	25.11	167.84	52.17	21.02	22.14	11.62	1.81	...[b]
48657.....	1.116	13.09	7.44	23.89	49.30	25.21	153.84	50.02	23.23	27.52	10.00	1.24	1.75
48658.....	1.132	24.74	9.01	27.63	48.39	16.69	138.25	56.72	29.22	32.18	6.34	1.52	...[b]
48659.....	1.147	42.49	22.34	28.26	51.41	13.63	127.94	52.32	26.00	15.79	13.80	7.99	7.13
48660.....	1.162	...[b]	20.22	29.05	58.69	40.07	120.13	51.86	18.71	34.85	18.73	8.47	4.30
48661.....	1.178	22.63	20.37	21.35	54.27	18.24	124.08	50.89	24.83	24.57	4.43	3.76	3.14
48662.....	1.193	15.87	6.64	21.33	45.60	22.93	100.29	40.89	12.54	28.17	6.73	9.45	3.05
48663.....	1.208	13.37	7.78	18.16	43.32	17.43	84.37	34.86	11.71	21.59	4.95	7.60	3.97
48667.....	1.391	7.09	4.07	19.76	27.58	10.32	40.32	19.23	11.46	17.67	0.91	2.86	...[b]
48668.....	1.407	2.58	5.06	17.48	26.41	9.81	45.68	21.40	9.70	16.23	4.87	3.85	2.32
48669.....	1.424	6.44	4.87	16.09	25.21	9.52	35.78	18.83	9.91	13.85	2.54	3.79	1.90
48670.....	1.443	6.40	4.30	17.01	25.21	11.12	37.82	17.33	10.78	14.15	2.02	3.03	1.84
48671.....	1.460	10.20	3.74	16.20	25.59	8.79	34.90	17.82	11.28	13.47	1.14	4.05	1.74
48672.....	1.477	11.07	8.95	16.04	24.07	11.96	39.53	13.37	9.80	10.58	2.98	1.07	5.20
48673.....	1.494	12.19	...[b]	20.07	27.19	12.81	32.66	12.34	16.10	16.23	6.09	3.35	1.25
48674.....	1.510	17.48	7.65	27.96	40.24	36.41	111.74	25.76	17.47	18.36	21.78	4.27	...[b]
48675.....	1.527	...[b]	11.01	13.01	25.25	8.87	27.97	21.26	12.17	15.24	12.71	3.50	2.66
48676.....	1.544	5.32	2.41	14.88	26.23	8.93	35.81	15.80	10.45	14.06	4.15	2.32	3.13
48677.....	1.564	3.29	3.34	16.92	23.03	7.69	33.13	18.47	10.08	14.94	2.65	4.67	4.23
48682.....	1.716	2.61	5.33	17.82	25.22	9.81	39.40	19.71	10.10	16.65	3.35	2.40	2.29
48683.....	1.734	4.52	6.31	18.01	29.05	10.45	42.23	21.06	12.39	12.89	4.01	3.13	2.25
48684.....	1.749	106.70	47.94	69.86	128.31	181.46	310.07	77.08	35.09	36.90	50.12	24.93	14.81
48685.....	1.765	30.31	20.17	37.80	92.36	82.98	372.15	76.76	25.93	41.90	37.42	14.91	4.61
48686.....	1.780	21.92	16.35	24.77	70.65	56.45	274.16	63.81	24.26	33.42	25.80	15.95	9.78

[a] Fluxes are in units of 10^{-13} ergs s^{-1} cm^{-2}.

[b] Not measurable.

TABLE 9

MEASURED VELOCITIES[a] OF GHRS EMISSION LINES

Ion	Phase	Wavelength	RV	ΔV[b]	Wavelength	RV	ΔV[b]	RV_K[c]	RV_G[c]
Si IV	1.67	1393.514	−51.9	6.4	1402.499	−57.9	0.3	−58.3	39.1
O IV]	1.67	1400.890	−56.9	1.3	...	...	...	−58.3	39.1
C IV	0.32	1548.378	34.1	4.4	1550.931	30.4	0.7	29.7	−70.8
C IV	1.57	1548.017	−35.8	0.2	1550.652	−23.6	12.0	−36.0	11.3
C IV	1.66	1547.977	−43.6	13.1	1550.533	−46.6	10.1	−56.7	37.1
C IV	1.95	1548.160	−8.1	22.2	1550.720	−10.4	19.8	−30.3	4.1
Si III]	0.35	1892.176	23.1	−1.9	...	...	...	25.0	−64.9
Si III]	1.22	1892.463	68.6	35.1	1892.484	72.0	38.5	33.5	−75.6
Si III]	1.60	1891.707	−51.2	−7.2	...	...	...	−44.0	21.3
Si III]	1.64	1891.674	−60.7	−7.6	...	...	...	−53.1	32.5
Si III]	2.00	1892.042	1.9	16.9	...	...	...	−15.0	−15.0
C III]	0.35	1908.890	24.5	−0.4	...	...	...	25.0	−64.9
C III]	1.22	1909.295	88.2	54.6	...	...	...	35.1	−75.6
C III]	1.60	1908.403	−52.0	−8.0	...	...	...	−44.0	21.3
C III]	1.64	1908.192	−85.2	−32.1	...	...	...	−53.1	32.5
C III]	2.00	1908.603	−20.6	−5.6	...	...	...	−15.0	−15.0

[a] In km s^{-1}.
[b] Relative to the K star.
[c] Using the orbital elements in Strassmeier et al. 1993.

off by more than a few km s^{-1}, so the large line shifts must be real and are likely due to the flare. The position of the narrow component (Table 9) implies a redshift of 38 km s^{-1} and 144 km s^{-1} with respect to the K or G star, respectively. Since the redshift is a combination of intrinsic flow and projected rotational velocities, the flare could have occurred on either or both stars.

3.5. *Simultaneous Photometry*

We display the contemporaneous visual band photometry in Figure 10. The V-band curve, which shows a single minimum around phase 0.5, is typical for this system (Rodonó & Cutispoto 1992). No conclusions regarding any correlation or anticorrelation between visual brightness and UV flux (e.g., Rodonó et al. 1987; Huenemoerder, Ramsey, & Buzasi 1990; Dempsey et al. 1993) is possible, because the system was in a UV-flaring state for a substantial fraction of the time. The mean visual brightness from Table 3 is 5.865 ± 0.03. This is the faintest the system has been in over 18 yr of photometric observations and consistent with the decreasing trend observed from 1990 to 1993 (Henry et al. 1995). Since decreased mean brightness likely indicates

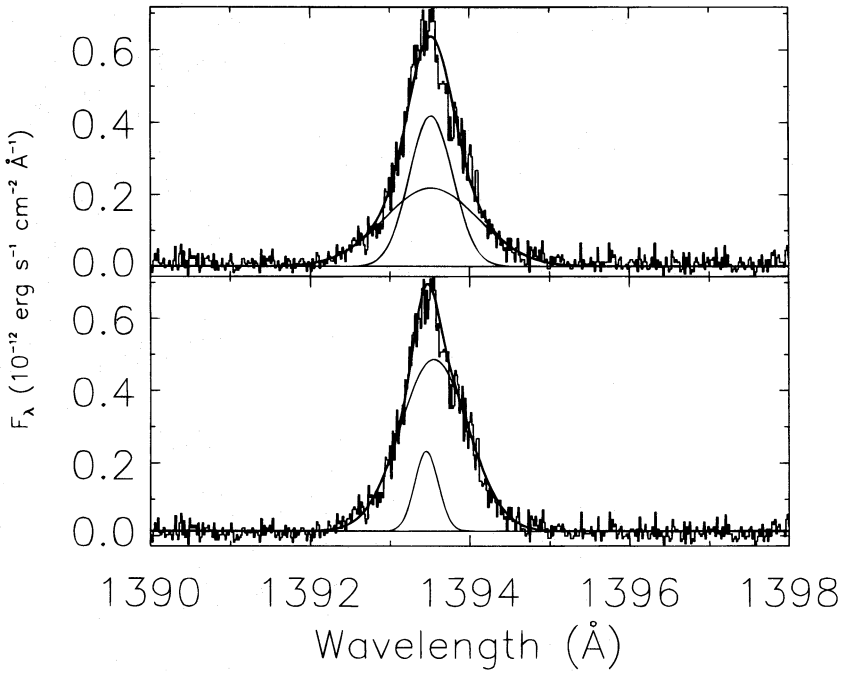

FIG. 8.—The Si IV 1393.8 Å line profile showing the fit by Wood et al. (*top panel*), which includes a narrower component (FWHM = 0.543 Å) ascribed to the global emission from the star and a broad component (FWHM = 1.115 Å) to account for the wings. The alternative fit shown in the lower panel, which fits the profile equally well, has a broad component of roughly the same width (FWHM = 1.001 Å) and an additional narrow component (FWHM = 0.350 Å) which is likely due to a flare with the same width for the global emission component. Note that the fit parameters in Tables 7 and 9 are single Gaussian component models.

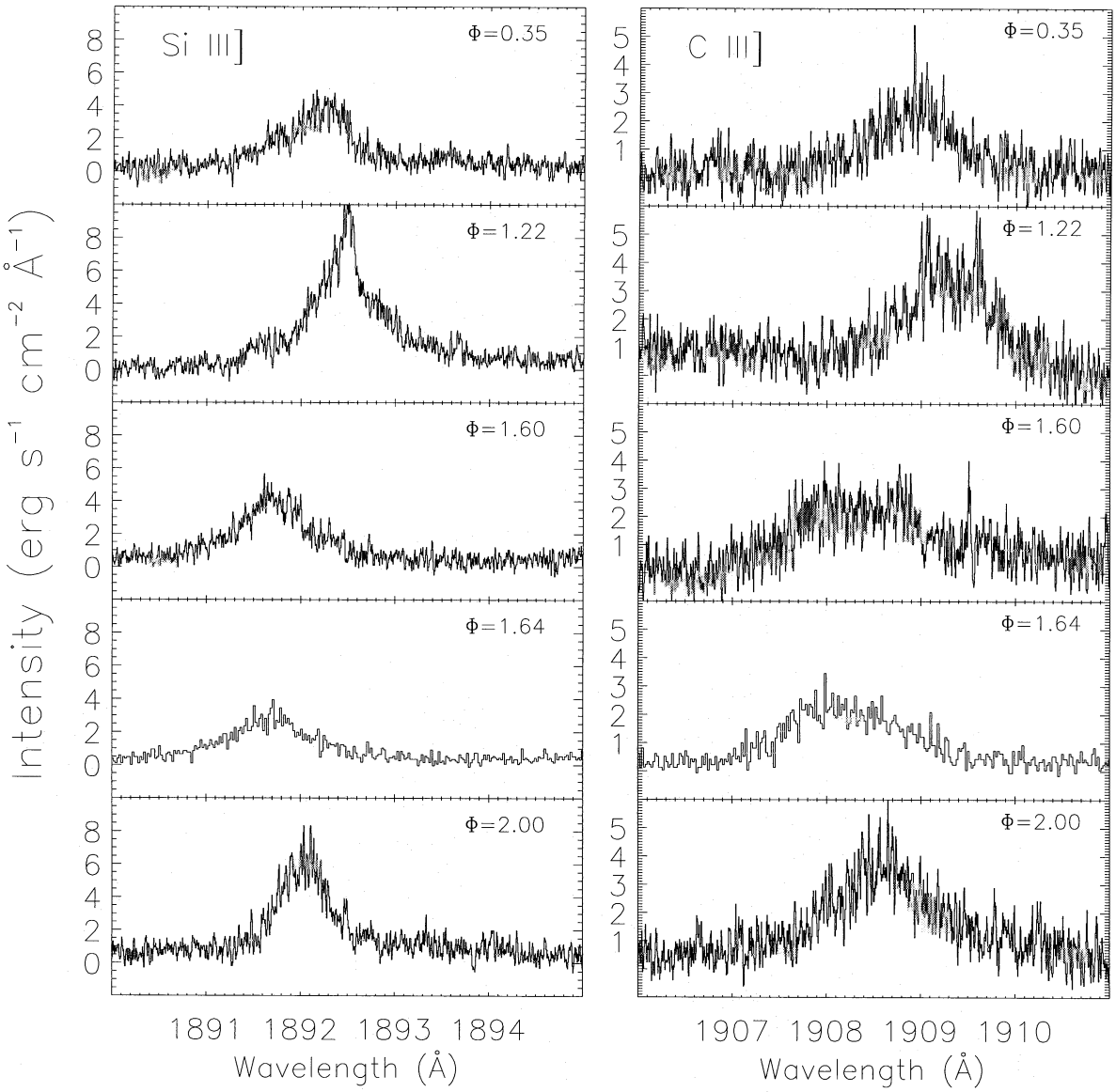

FIG. 9.—The density sensitive lines, Si III] and C III]. The observation at phase 1.22 is with the G200M grating while the others are Echelle-B spectra. The Si III] profile at 1.22 is profoundly affected by the flare, while the C III] profile at the same phase is relatively unaffected, indicating a high-density flaring region.

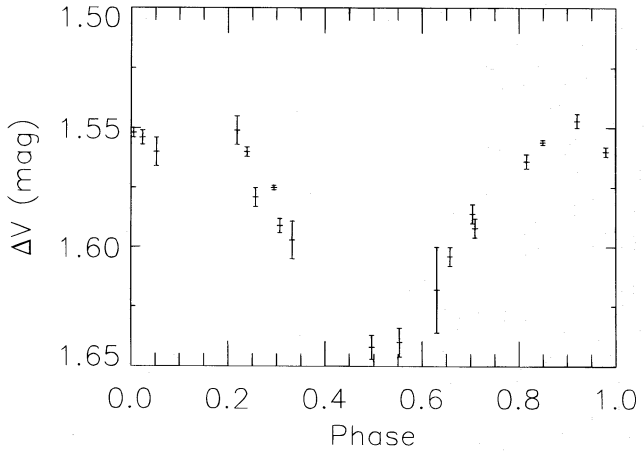

FIG. 10.—Visual photometry obtained 1993 September 3–October 8. For comparison with the ultraviolet observations, these data are folded against the orbital phase. The light minimum around phase 0.5 is likely due to a maximum starspot coverage at that phase.

increased photospheric spot coverage, it may not be surprising that V711 Tau was undergoing a major episode of flaring activity in 1993 September.

4. DISCUSSION

One of the initial goals of this program was to study the variability of V711 Tau induced by surface inhomogeneities of the emission lines as the stars rotate. Phase coverage is not adequate in the high-resolution GHRS data for detailed surface modeling as done by Neff et al. (1989). To do so requires that at least eight unique phases be observed and that repeated coverage be obtained at the same phase on different rotational cycles. As a further complication, V711 Tau appears to have been undergoing a significant amount of flaring (Figs. 5 and 6).

As indicated in Figure 3, the Mg II emission lines cannot be simply modeled by two Gaussians, one each for the K and G star, but to extract more information from the profile

(e.g., plage signatures) the broad wings must be properly characterized. In the basic two-component model, the extended wings appear to be distributed symmetrically about the velocity of the K star. However, the presence of a similar component in the G-star profile could easily be missed with the S/N and phase coverage of our data. The large variations in the Mg II flux residuals (e.g., -0.22 to 6.04×10^{-12} ergs s^{-1} cm^{-2} for the k line) suggest that much of the observed variability results from the changes in the line wings.

A different picture emerges if the Mg II profile is modeled with three components, one each for the K and G star and a third for the broad component of the K star. All three components show marked variations. Adding a broad component shifts a large amount of flux from the global stellar components into the broad feature. Through radiative transfer calculations, Wood et al. (1996) were able to reproduce the Mg II profiles with some success. Although the theoretical profiles also had broad wings, they are still not as broad as observed (see Fig. 15 in Wood et al.). In this case, additional broadening (e.g., microflaring in the chromosphere) is required to explain the extended wings.

Based on GHRS observations of the Fe XXI and O V lines in V711 Tau, Robinson et al. (1996) discuss various mechanisms that could lead to the extended wings. They observed a relatively small amount of nonthermal broadening in the Fe XXI line, which is not what would be expected if the corona was heated by microflares. Based on detailed models of the O V line in V711 Tau, they concluded that the broadening most likely arises from MHD turbulence that is generated by nonlinear Alfvén waves. Since the broad wings are seen only in the transition region lines and not in the coronal features like Fe XXI (Wood et al. 1996; Robinson et al. 1996), it appears that most of this turbulence is produced in the transition region.

Robinson et al. (1996) also fitted the O V line with broad and narrow Gaussian components. As in our fits, they find no significant velocity difference between the two components, in contrast to the models in Wood et al. (1996). However, the width of their narrow component (65 km s^{-1}) is significantly narrower than most found by Wood et al.

With V711 Tau flaring so much during the observations, it is not clear whether the extended wings result solely from flares or from a steady state mechanism such as microflaring or non-LTE effects. The former scenario is supported by the unusual Mg II profile at phase 1.97. Detection of broad wings in other stars (Linsky & Wood 1994; Linsky et al. 1995; Wood et al. 1996) come from single-epoch observations without supporting data from other wavelength regions or photometry. Therefore, the flare state of the system was unknown at the time of those observations. Further observations of V711 Tau in quiescence will be required to determined if the extended wings are transient or not.

Due to centering problems in the aperture, the *HST* C IV fluxes are not reliable. Combined with poor phase sampling, we can say little about these data. However, the *IUE* C IV fluxes clearly show the two large flares around phases 1.1 and 1.8 that were observed in the Mg II lines. A weaker, shorter lived flare, that is not seen in the Mg II flux, was also detected near phase 1.5.

Based on the relative contribution of each star to the combined Mg II flux, we expect the G star to contribute approximately 7% of the flux at C IV. From our modeling, the G star likely accounts for 8%–15% of the line flux. Unless we can independently constrain the contributions from either star, we cannot say anything more definitive since the outcome is highly model dependent. The nonuniqueness of these modeling schemes is illustrated by the vastly different fits that can be derived for the Si IV line (see Fig. 8).

As with the Mg II and C IV lines, we see a large degree of variability in the Si III] and C III] lines, both in total flux and in line shape. The largest observed value of N_e was observed at phase 1.22 where both the Mg II and C IV flux are in a flare state. The Si III] profile at this phase is clearly different in shape then at the other phases.

Support for this work for R. C. D., J. L. L., and J. E. N. was provided by NASA through grant numbers GO-4447.03-92A, S-56460-D, GO-4447.02-92A, respectively, from the Space Telescope Science Institute, which is operated by Association of Universities for Research in Astronomy, Incorporated, under NASA contract NAS5-26555. Additional support for J. E. N. was provided by NASA grants NAGW-2603 and NAG5-2118. A. B. was supported by NASA grants NAG5-985 and NAG5-2259 to the University of Colorado. M. J. T. acknowledges support of the University Scholars Program at Penn State. The analysis of the flares on V711 Tau form the basis of her undergraduate Honor's thesis. The authors wish to thank J. Scott and R. Robinson for their helpful suggestions.

REFERENCES

Ayres, T. R., Marstad, N. C., & Linsky, J. L. 1981, ApJ, 247, 545
Baliunas, S. L., & Dupree, A. K. 1982, ApJ, 252, 668
Bevington, P. R. 1969, in Data Reduction and Error Analysis for the Physical Science (New York: McGraw-Hill)
Blackwell, J., Shore, S. N., Robinson, R. D., Feggans, K., Lindler, D., Malumuth, E., Sandoval, J., & Ake, T. B. 1993, in A User's Guide to the GHRS Software Version 2.1, GHRS internal document
Brandt, J. C., et al. 1994, PASP, 106, 890
Crutcher, R. M. 1982, ApJ, 254, 82
Dempsey, R. C., Bopp, B. W., Henry, G. W., & Hall, D. S. 1993, ApJS, 86, 293
Dempsey, R. C., Bopp, B. W., Strassmeier, K. G., Granados, A. F., Henry, G. W., & Hall, D. S. 1992, ApJ, 392, 187
Donati, J.-F., Brown, S. F., Semel, M., Rees, D. E., Dempsey, R. C., Matthews, J. M., Henry, G. W., & Hall, D. S. 1992, A&A, 265, 682
Dorren, J. D., & Guinan, E. F. 1990, ApJ, 348, 703
Duncan, D. K. 1992, in Goddard High Resolution Spectrograph Instrument Handbook, Version 3.0 (Baltimore: Space Telescope Science Inst.)
Gibson, D. M., Hjellming, R. M., & Owen, F. N. 1975, ApJ, 200, L99
Hallman, K. L., Altner, B., & Endal, A. S. 1991, ApJ 372, 610
Heap, S. R., et al. 1995, PASP, 107, 871
Henry, G. W., Eaton, J. A., Hamer, J., & Hall, D. S. 1995, ApJS, 97, 513
Huenemoerder, D., Ramsey, L., & Buzasi, D. 1990, ApJ, 350, 763
Hulbert, S. J., & Baggett, W. E. 1993, in Calibrating the *Hubble Space Telescope*, ed. J. Chris Blades & Samantha J. Osmer (Baltimore: Space Telescope Science Inst.), 336
Jones, K. L., Brown, A., Stewart, R. T., & Slee, O. B. 1996, MNRAS, submitted
Kürster, M., & Schmitt, J. H. M. M. 1996, A&A, in press
Linsky, J. L. 1990, in Active Close Binaries, ed. C. Ibanoğlu (Doredrecht: Kluwer), 747
Linsky, J. L., Neff, J. E., Brown, A., Gross, B. D., Simon, T., Andrews, A. D., Rodonó, M., & Feldman, P. A. 1989, A&A, 211, 173
Linsky, J. L., Wood, B. E., Judge, P., Brown, A., Andrulis, A., & Ayres, T. 1995, ApJ, 442, 360
Linsky, J. L., & Wood, B. E. 1994, ApJ, 430, 342
Marstad, N., et al. 1982, in Advances in UV Astronomy: Four Years of *IUE* Research (NASA CP-2238), ed. Y. Kondo et al. (Washington: NASA), 554
Murthy, J., Henry, R. C., Moos, H. W., Landsman, W. B., Linsky, J. L., Vidal-Madjar, A., & Gry, C. 1987, ApJ, 315, 675
Neff, J. E. 1987, Ph. D. thesis, Univ. of Colorado, Boulder

Neff, J. E. 1991, Mem. Soc. Astron. Ital., 62, 291
———. 1995, in IAU Symp. 176, Stellar Surface Structure, ed. K. Strassmeier (Dordrecht: Kluwer), in press
Neff, J. E., et al. 1996, in preparation
Neff, J. E., Walter, F. M., Rodonò, M., & Linsky, J. L. 1989, A&A, 215, 79
Piskunov, N., Wood, B. E., Linsky, J. L., Dempsey, & Ayres, T. R. 1996, ApJ, submitted
Ramsey, L. W., & Nations, H. L. 1980, ApJ, 239, L121
Robinson, R. D., Airapetian, V. S., Maran, S. P., & Carpenter, K. G. 1996, ApJ, in press
Rodonó, M., et al. 1987, A&A, 176, 267
Rodonó, M., & Cutispoto, G. 1992, A&AS, 95, 55
Simon, T., & Linsky, J. L. 1980, ApJ, 241, 759
Soderblom, D. S., Sherbert, L. E., & Hulbert, S. J. 1993, in Calibrating the *Hubble Space Telescope*, ed. J. C. Blades & S. J. Osmer (Baltimore: Space Telescope Science Inst.), 264
Strassmeier, K. G., Hall, D. S., Fekel, F. C., & Scheck, M. 1993, A&AS, 100, 173
Vogt, S. S., & Penrod, D. 1983, PASP, 95, 565
Wahlgren, G. M., Leckrone, D. S., Shore, S. N., Lindler, D. J., Gilliland, R. L., & Ebbets, D. C. 1991, ApJ, 377, L41
Walter, F. M. 1995, in IAU Symp. 176, Stellar Surface Structure, ed. K. Strassmeier (Dordrecht: Kluwer), in press
Walter, F., Charles, P., & Bowyer, S. 1978, ApJ, 225, L119
Walter, F. M., Neff, J. E., Gibson, D. M., Linsky, J. L., Rodonó, M., Gary, D. E., & Butler, C. J. 1987, A&A, 186, 241
Wood, B. E., Harper, G. M., Linsky, J. L., & Dempsey, R. C. 1996, ApJ, 458, 761
Zirin, H. 1988, in The Astrophysics of the Sun (New York: Cambridge Univ. Press), 317